PHYSICAL REVIEW E **76**, 066401 (2007)

Long- and short-lived electrons with anomalously high collision rates in laser-ionized gases

Tobias Kampfrath,[1,*] Dirk O. Gericke,[2] Luca Perfetti,[1] Petra Tegeder,[1] Martin Wolf,[1] and Christian Frischkorn[1]
[1]*Fachbereich Physik, Freie Universität Berlin, Arnimallee 14, 14195 Berlin, Germany*
[2]*Centre for Fusion, Space and Astrophysics, Department of Physics, University of Warwick, Coventry CV4 7AL, United Kingdom*

(Received 9 August 2007; published 6 December 2007)

Ultrashort broadband terahertz pulses are applied to probe the electron dynamics of gaseous Ar and O_2 following ionization by an intense femtosecond laser pulse. The conductivity in the plasma center is extracted by a modified Wentzel-Kramers-Brillouin approach. It exhibits a nearly perfect Drude-like spectral shape and yields the temporal evolution of the free-electron density and collision rate. While the electron density in the Ar plasma remains nearly constant during the first 200 ps after generation, it decays much faster in O_2 due to dissociative recombination which is only possible in molecular plasmas. Adding a small amount of the electron scavenger SF_6 to Ar reduces the electron lifetime in the plasma dramatically and allows us to determine the electron temperature to about 20 000 K. Furthermore, anomalously high, metal-like electron collision rates of up to 25 THz are found. Kinetic plasma theory substantially underestimates these rates pointing towards additional and more complex processes randomizing the total electronic momentum. Our results are relevant to both lightning control and generation of terahertz radiation by intense laser pulses in gases.

DOI: 10.1103/PhysRevE.76.066401 PACS number(s): 52.50.Jm, 34.80.Lx, 51.50.+v, 52.20.Fs

I. INTRODUCTION

Free charge carriers in gases play an important role in everyday life, for instance, in fluorescence tubes, lightnings during a thunderstorm, and sparks in electrical equipment. Both from an application-oriented and a fundamental point of view, it is imperative to understand the involved electron dynamics. For example, triggering lightnings in the atmosphere in a controlled way has been a longstanding dream [1]. To this end, laser pulses are suggested to produce a channel of ionized air between the ground and the clouds which should lead to a controlled discharge. The potential of this scheme has been demonstrated in laboratory over distances of a few meters [2]. In order to cover much larger distances, knowledge on the lifetime and mobility of the induced free electrons is highly desirable.

In contrast to this situation where sufficiently *long*-lived charge carriers are essential, free electrons in high-voltage devices should be as *short*-lived as possible to prevent sparks, short circuits, and material corrosion. For this reason, the devices are often purged with insulating gases such as the electron scavenger SF_6 which efficiently quench any nascent discharge [3]. Detailed knowledge of the charge-carrier dynamics is essential for a microscopic understanding of relevant elementary processes like free-electron formation, loss, and scattering. Therefore, one has to gain insights into the dynamics of plasma quantities like electron density, collision rate, and temperature.

Femtosecond time-resolved studies of gas plasmas employ a powerful and short laser pulse to ionize a gas followed by a probe pulse. Several methods have been used to monitor the free-electron dynamics of the resulting plasma. Interferometrical [4] and diffractive [5] schemes with visible probe pulses, in principle, yield the free-electron density n_e. However, the electron collision rate Γ is much more difficult to obtain since absorption effects are weaker than phase-shift effects by a factor $\Gamma/\omega \sim 10^{-2}$ for visible probe radiation of frequency ω. One further approach is to detect the total light emission of a plasma that was re-excited by a delayed probe pulse [6]. However, this technique is quite indirect since the functional relation between emitted light intensity and plasma quantities such as n_e is not known.

Instead, terahertz (THz) radiation is a promising alternative probe because Γ and the electron plasma frequency $\Omega_{pl} = \sqrt{4\pi e^2 n_e / m_e}$ of optically ionized gases lie in the THz range. For example, the plasma frequency of a plasma consisting of electrons and singly ionized molecules with a number density of ambient air is $\Omega_{pl}/2\pi \approx 45$ THz. THz spectroscopy in the 1 to 3 THz frequency range has already proven to be useful in the characterization of discharge plasmas in He [7] and Ar [8], however, with a limited temporal resolution in the nanosecond range. The same technique was also used to gain insights into the mechanism of the laser-induced ionization of O_2 with picosecond resolution [9]. Previously, we used time-resolved THz spectroscopy to observe the ultrafast capture of free electrons by the electron scavenger SF_6 [10].

In this contribution, we investigate the ultrafast electron dynamics in laser-ionized O_2 and Ar gases employing THz probe pulses covering the frequencies from 10 to 25 THz. These *higher* frequencies allow us to extend the electron-density range up to $n_e \sim 10^{18}$ cm^{-3} since plasmas are only transparent above the plasma frequency Ω_{pl}. The measured plasma response is excellently described by both the Drude model and a microscopic approach based on the Boltzmann equation. Fitting gives the temporal dynamics of the free-electron density n_e and the electron collision rate Γ. We observe a completely different relaxation behavior in Ar compared to O_2: The decay of the free-electron density in O_2 is substantially faster than in Ar due to dissociative recombination which is only possible in molecular plasmas. Adding a small amount of the electron scavenger SF_6 reduces the electron lifetime in the Ar plasma dramatically and allows us

---

*tobias.kampfrath@physik.fu-berlin.de

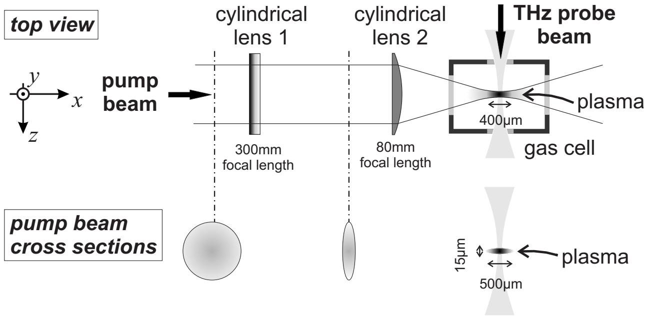

FIG. 1. Schematic of the sample geometry. The pump beam is focused into the gas cell by two cylindrical lenses in orthogonal orientation. The resulting plasma sheet around the focal plane of lens 2 is probed by the THz beam perpendicular to the pump beam.

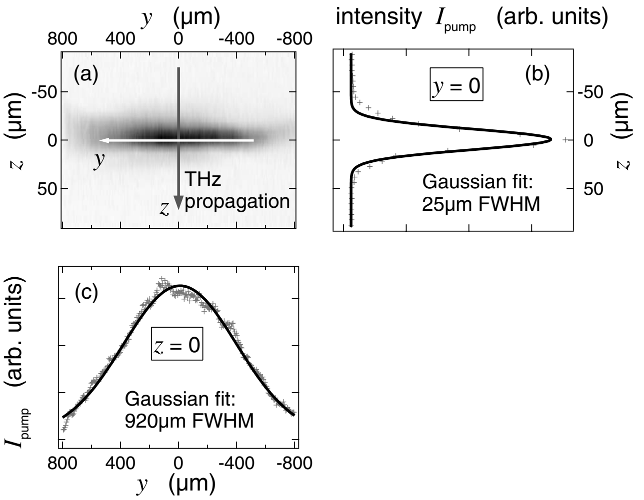

FIG. 2. (a) Grayscale plot of the intensity profile I_{pump} of the pump-beam focus as measured with a charge-coupled device (CCD) camera. The THz probe pulse propagates along the z axis. Note the different axis scaling. (b), (c) Line plots of I_{pump} along the z and y axis in (a), respectively. With a 400-μm length of the pump focus in x direction, the THz probe beam sees a plasma sheet homogeneous in the x-y plane.

determine the electron temperature to about 20 000 K. Furthermore, strikingly high electron collision rates are found in all gases. The peak values of this key quantity for electron transport are comparable to metals and significantly underestimated by state-of-the-art theoretical models. This behavior possibly originates from the large spatial gradients in our plasma.

II. EXPERIMENT AND DATA ANALYSIS

A. Experimental details

Our setup employs ultrashort light pulses (center wavelength 800 nm, pulse energy 0.6 mJ, pulse duration 20 fs, repetition rate 1 kHz) from an amplified Ti:sapphire laser system (Femtolasers Femtopower Pro). 90% of the laser power is focused into a gas cell by two cylindrical lenses whose symmetry planes are perpendicular to each other as schematically shown in Fig. 1. The gas is ionized around the focal plane of the second lens on a length of roughly 400 μm. The beam cross section at this position resembles a strongly elongated ellipse as shown by the measured pump-intensity profile I_{pump} in Fig. 2(a). Along the z axis, I_{pump} is a Gaussian

$$I_{\text{pump}}(z) \propto \exp\left[-4\ln 2\frac{z^2}{w^2}\right] \tag{1}$$

with a full width at half maximum (FWHM) of only $w = 25\ \mu$m, see Fig. 2(b), in contrast to the much larger width of 920 μm along the y axis, see Fig. 2(c). As shown in Appendix B, the linear dimensions of the plasma are roughly half as large as the dimensions of the pump-beam focus.

The THz probe beam travels perpendicularly to the pump beam along the z direction and is focused into the plasma. The resulting THz beam waist of 50 μm is much smaller than the transverse plasma dimensions such that the THz beam probes a transversely homogeneous plasma sheet. The THz pulses are obtained from the residual 10% of the amplifier output by difference-frequency generation in a 60-μm thick GaSe crystal [11]. The time-dependent THz electric field is detected by electro-optic sampling [12] using the 12-fs pulses of the seed laser [13] and a 300-μm thick ZnTe crystal [14]. As shown in Fig. 3, the THz pulses have a duration of about 100 fs and cover the spectral range from 10 to 25 THz. An acousto-optic pulse shaper [15] between the seed laser and the amplifier stage is employed to maximize the bandwidth of the THz pulses and the plasma-induced signal. We verified that the latter did not depend on the THz intensity showing that the THz pulse can be still considered as a linear probe despite its high electric fields [13]. A temporal resolution of about 200 fs is achieved in our setup which is estimated by the rise time of the pump-induced signal as shown in Fig. 4. This is not determined by the THz pulse duration but rather by the 90° geometry of pump- ver-

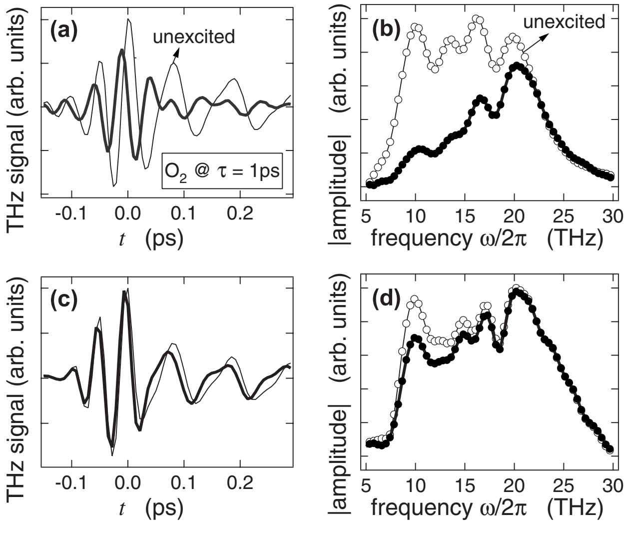

FIG. 3. (a) THz waveforms $S_\infty(t)$ and $S_\tau(t)$ transmitted through unexcited and excited O_2, respectively, at a pump-probe delay of $\tau = 1$ ps and a peak pump intensity of about 3×10^{13} W cm^{-2}. (b) Amplitude spectra of the waveforms $S_\infty(t)$ and $S_\tau(t)$ in panel (a). (c), (d) Same as (a), (b) but for a pump intensity reduced by $\approx$30%.

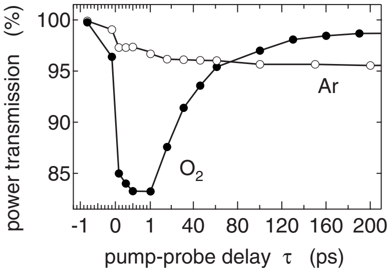

FIG. 4. Fraction of the THz pulse energy transmitted through Ar and O_2 as a function of the pump-probe delay τ. Note the expanded τ-axis scaling around zero delay.

sus probe-beam propagation: Different sample positions along the x direction of Fig. 1 are excited at different times, and it takes the pump pulse 50 μm/$c \approx 200$ fs to traverse the probe-beam diameter.

The gas under investigation enters the gas cell at a pressure slightly above the ambient pressure of 1 bar at the cell outlet, in order to guarantee a fresh sample for each laser shot. Glass and Si windows are used for access of the 800-nm and THz radiation, respectively. We use O_2, Ar, and SF_6 with a purity of 99.9, 99.998, and 99.99%, respectively, and in addition an Ar:SF_6 mixture with a 9:1 mixing ratio.

B. Elementary processes involved

Before experimental data are presented, we briefly summarize the mechanism of plasma generation by intense laser pulses as well as subsequent relaxation processes that are relevant to our experiment.

1. Optical ionization

From the O_2, Ar, and SF_6 ionization potentials of $V_{\text{ion}} = 12.1$, 15.8, and 15.3 eV [16], respectively, and a peak intensity of roughly 10^{14} W cm^{-2} in the focus of the linearly polarized pump beam, we expect single ionization to be the main mechanism of ionization in our experiment. The ionization process can be qualitatively characterized by the Keldysh parameter [17]

$$\gamma_K = \sqrt{\frac{V_{\text{ion}}}{2V_p}}. \tag{2}$$

Here, $V_p = e^2|E_0^2|/4m_e\omega_{\text{pump}}^2$ is the ponderomotive potential that equals the kinetic energy of an electron accelerated to the quiver velocity $e|E_0|/m_e\omega_{\text{pump}}$ by the pump electric field having frequency ω_{pump} and amplitude E_0. For weak fields, that is $\gamma_K \gg 1$, the ionization can be described by multiphoton absorption based on higher-order perturbation theory [17]. At Keldysh parameters of $\gamma_K \approx 1$ and linearly polarized light, the laser field starts to compensate the electric field of the nucleus such that bound electrons tunnel into free states. In the limit $\gamma_K \ll 1$, the Coulomb barrier is so low that the electron can escape classically [18].

At our pump photon energy of $\hbar\omega_{\text{pump}} = 1.55$ eV, the crossover region with $\gamma_K \approx 1$ is reached for most gases at laser intensities of 10^{14} W cm^{-2}. For the largest pump-pulse energies of 0.4 mJ in our experiment, we estimate a peak intensity of 3×10^{13} W cm^{-2} corresponding to a Keldysh parameter of $\gamma_K \approx 15$. This indicates that the regime of field ionization is not yet completely reached. Moreover, measurements of the yield of N_2^+, N_2^{2+}, and N^+ ions as a function of the laser intensity by Cornaggia *et al.* [19] show that about 99% of all ions in our plasmas must be singly charged.

2. Plasma relaxation

After plasma generation, the free electrons (e) thermalize on a subpicosecond time scale by e-e scattering [20,21]. We can therefore safely assume a Maxwell-Boltzmann distribution for the electrons. Subsequently, they cool via energy transfer to the ions (i). For the nondegenerate and weakly coupled plasmas investigated here, binary collisions dominate this process, and the equilibration time can be estimated by the Spitzer formula [22,23] or more rigorous treatments [24–26]. All approaches predict an electron cooling on the nanosecond time scale for our plasmas. Cooling by energy transfer to the neutral particles (n) is less important, especially in noble gases due to the much smaller cross sections for e-n scattering [27].

Free-electron decay by e-i recombination is another potential relaxation process. In order to conserve both total energy and momentum, this process requires an additional energy sink that is provided by internal degrees of freedom or a third particle such as another electron or an emitted photon.

Finally, plasma expansion is one further relaxation process to be considered. However, the expansion velocity of our plasmas is limited by the ion sound speed $\sqrt{k_B T_e / m_i}$. With an electron temperature of $k_B T_e \approx 2$ eV derived from our data in Sec. IV A 3, we expect our plasmas to expand less than a few μm over the 200-ps time range of the measurement. This length is small compared to the 15-μm thickness of the plasma, see Sec. II A, such that we can neglect transport effects. These estimates are consistent with measurements of the expansion of a laser-generated plasma channel in a N_2 gas jet by Dunne *et al.* [28], where a 10-μm expansion in 200 ps was found, however, for a 10 times larger electron temperature and a 100 times smaller gas density. Therefore, mean free path and expansion velocity must be greatly reduced in our plasmas leading to an expansion of much less than 10 μm within 200 ps.

C. Raw data

For each gas, we take THz waveforms $S_\tau(t)$ at various delays τ between pump and probe pulse where t denotes the "local" time of the THz pulse referenced to the signal maximum at $t=0$. Simultaneously, we also acquire waveforms $S_\infty(t)$ for an unexcited gas which is achieved by blocking every second pump pulse. The signal $S_\tau(t)$ reflects the true electric field of the THz pulse quite well since the response of our relatively thick detection crystal is spectrally flat [14].

Figure 3(a) shows THz waveforms for unexcited and excited O_2 at a peak pump intensity of about 3×10^{13} W cm^{-2}. Note that parts of the THz pulses arrive earlier at the detector when the sample is excited. This temporal shift is an optical fingerprint of free charge carriers which lead to a refractive index n_τ with Re $n_\tau < 1$ and consequently a phase velocity above the vacuum speed of light. In addition, the THz signal is smaller for the excited sample. The amplitude spectra of S_τ and S_∞ in Fig. 3(b) reveal that this amplitude reduction is larger for smaller probe frequencies, which is a further signature of free-carrier absorption, as will be discussed in Sec. III. Figures 3(c) and 3(d) finally show S_τ and S_∞ in the time and frequency domain for a 30% decreased pump intensity. Although the pump-induced effects are now smaller than in Figs. 3(a) and 3(b), all following data are taken for this lower pump intensity in order to run the laser system well below the damage threshold.

In order to get an idea of the time scales of the plasma dynamics, Fig. 4 presents the total THz pulse energy transmitted through O_2 and Ar as a function of the pump-probe delay τ. It displays strikingly different dynamics for both gas species: While the drop in the transmission occurs instantaneously within the temporal resolution of 0.2 ps for both O_2 and Ar, the THz transmission recovers considerably faster for O_2 than for Ar.

D. Extraction of the dielectric function

In general, the interaction between the sample gas and the pump pulse leads to temporary changes in the conductivity σ_τ of the sample where τ is the time passed since arrival of the pump pulse. In the following, we prefer the use of the dimensionless dielectric function $\varepsilon_\tau = 1 + 4\pi i \sigma_\tau / \omega$. The dielectric function represents the maximum information that can be obtained with a linear electromagnetic probe. At THz frequencies, knowledge of the dielectric function allows for important conclusions about the electron dynamics in the plasma. Therefore, a reliable extraction of ε_τ from the measured waveforms is mandatory.

Due to the pump-induced changes in the sample conductivity, the probing THz electric field $\boldsymbol{E}_\tau$ induces an additional current density [29]

$$\Delta \boldsymbol{j}_\tau(\boldsymbol{x},\omega) = \frac{\omega}{4\pi i} \Delta\varepsilon_\tau(\boldsymbol{x},\omega) \boldsymbol{E}_\tau(\boldsymbol{x},\omega), \tag{3}$$

where $\Delta\varepsilon_\tau = \varepsilon_\tau - \varepsilon_\infty$ is the pump-induced change in the dielectric function. To arrive at Eq. (3), we have applied a Fourier transformation from the time (t) to the frequency (ω) domain and made the following assumptions: (i) The THz current at position $\boldsymbol{x}$ is exclusively generated by the electric field at the same position. Such local description is not sufficient for highly reflecting plasmas, where the probing field induces a current beyond its penetration depth [30]. However, this so-called anomalous skin effect does not occur in our plasmas since they exhibit a considerable transmission as indicated by Fig. 4. (ii) The sample responds quasi-statically and changes its dielectric function only slowly within the probe-pulse duration. This is fulfilled in our experiment for pump-probe delays $\tau > 0.2$ ps, see Fig. 4. Otherwise, strong frequency-mixing effects may occur which also make the use of quasistatic models for the dielectric function, like those in Sec. III, questionable [31,32,29]. (iii) The sample is locally isotropic which simplifies $\Delta\varepsilon_\tau$ to a scalar. This condition is usually fulfilled in gases although the pump pulse may induce some anisotropy. However, the latter should vanish on the subpicosecond time scale of electron thermalization, see Sec. II B 2.

Furthermore, the probe pulse $\boldsymbol{E}_\tau$ sees a transversely homogeneous sample since it propagates along the z direction in Fig. 1 perpendicularly to the plasma sheet. Then, Maxwell equations together with Eq. (3) reduce to a one-dimensional linear wave equation [29]

$$[\partial_z^2 + k_\tau^2(z,\omega)] E_\tau(z,\omega) = 0 \tag{4}$$

for any transverse field component E_τ, and with

$$k_\tau^2(z,\omega) = \frac{\omega^2}{c^2} [\varepsilon_\infty(z,\omega) + \Delta\varepsilon_\tau(z,\omega)] \tag{5}$$

as the squared local wave vector and $\varepsilon_\infty = 1$.

In order to extract $\Delta\varepsilon_\tau$ from the measured waveforms S_τ and S_∞ with the aid of Eq. (4), one has to consider the following complications: (i) The excitation of the gas is quite inhomogeneous along the THz propagation direction z as demonstrated by Fig. 2(b). Therefore, standard Fresnel formulas for homogeneous films are not applicable here [33]. Moreover, the pump-induced effects on the THz probe pulse are quite substantial, as can be seen from Fig. 3. Therefore, first-order perturbation theory may not be sufficient for a quantitative treatment of $\Delta\varepsilon_\tau(z,\omega)$ [29]. (ii) The spatial structure of the plasma along the z direction in Fig. 2(b) is unknown.

As detailed in Appendix A, concern (i) can be adequately overcome by a modified Wentzel-Kramers-Brillouin (WKB) approach. It leads to an expression for the relative change $\Delta E_\tau(z,\omega)/E_\infty(z,\omega)$ in the transmitted THz electric field, see Eq. (A6). Note that the measured THz signals ΔS_τ and S_∞ are a result of the THz propagation from the sample to the detector and the electro-optic detection process. However, these effects cancel out in the division such that one simply has

$$\frac{\Delta E_\tau(z_1,\omega)}{E_\infty(z_1,\omega)} = \frac{\Delta S_\tau(\omega)}{S_\infty(\omega)}, \tag{6}$$

where z_1 is a point behind the ionized region.

In order to account for complication (ii), Appendix B shows that the profile of $\sqrt{\varepsilon_\tau} - \sqrt{\varepsilon_\infty}$ along the z direction can be related to the pump-intensity profile of Eq. (1) by a simple power law. This procedure is justified by a consistent description of all experimental data with respect to the spectral and pump-intensity dependence.

Applying the resulting Eq. (B4) to our data, we obtain the dielectric function of O_2 and Ar at various pump-probe delays τ as shown in Fig. 5. The real part of $\Delta\varepsilon_\tau$ is negative for both the Ar and O_2 plasma, and decreases with decreasing frequency which is a clear signature of free charge carriers [29,34]. While for longer delays of $\tau > 100$ ps the $\Delta\varepsilon_\tau$ of Ar remains virtually unchanged, its magnitude for O_2 has already significantly decreased which underlines the different behavior of both plasmas, as seen in Fig. 4.

III. PLASMA CONDUCTIVITY

Now that we have extracted the dielectric function from our data, it has to be related to important plasma parameters

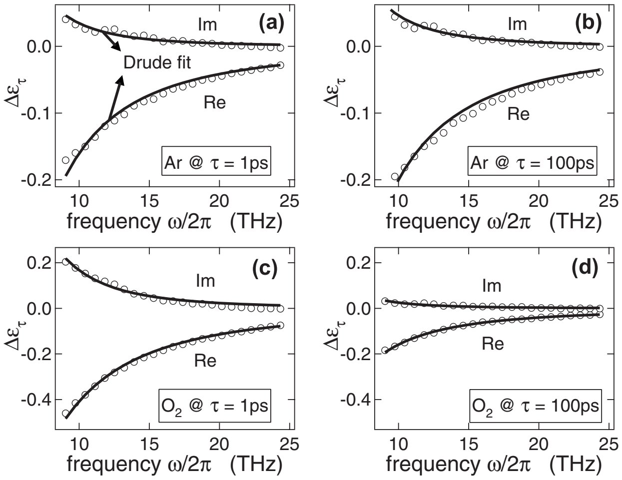

FIG. 5. (a) Pump-induced changes $\Delta\varepsilon_\tau$ in the dielectric function of Ar at $\tau = 1$ ps and (b) $\tau = 100$ ps after ionization which is nearly identical with (a). (c), (d) Same as (a), (b) for O_2. Note the different axis scaling and the strongly decreased dielectric function in (d). In all cases, the Drude model excellently reproduces the experimental data.

such as the free-electron density n_e and temperature T_e.

The dielectric function or, equivalently, conductivity quantifies how easily an applied electric field can induce a current in our gas sample. After optical ionization, the latter contains free electrons, ions, and neutral particles. Due to their small mass and their arbitrarily small excitation energies, the free electrons are expected to make the dominant contribution to the THz conductivity. Note that excitation energies of bound electrons are far above our probe photon energies of $\hbar\omega \sim 0.1$ eV.

The following sections present different models of the plasma conductivity and their application to our data.

A. Phenomenological Drude model

The Drude model considers free electrons that are accelerated by an applied electric field. However, their acquired velocity is completely randomized in a collision with obstacles where the mean collision rate Γ is a free parameter. The Drude model leads to the dielectric function [35,36]

$$\varepsilon^{D}(\omega) = 1 - \frac{\Omega_{pl}^2}{\omega^2 + i\Gamma\omega} \tag{7}$$

with the plasma frequency $\Omega_{pl} = \sqrt{4\pi n_e e^2 / m_e}$ and the free electron density n_e. Although the Drude formula is based on an extremely simplified model, it often provides a good *phenomenological* description of the low-frequency optical properties of metals [37] and doped semiconductors [38].

Figure 5 shows that the Drude formula yields excellent fits to our data. For this reason, we will subsequently use the Drude formula to parametrize our data by just two quantities, n_e and Γ. The next section summarizes a more sophisticated model which delivers a Drude-like conductivity and provides a microscopic interpretation of Γ. Moreover, we show that the Drude model accurately reproduces the magnitude of the electron density n_e.

B. Microscopic Boltzmann approach

In a semiclassical approach for locally homogeneous systems, the free electrons can be described by a distribution function $f(\boldsymbol{v}, t)$ where $\boldsymbol{v}$ is the electron velocity. The dynamics of f in an external electric field $\boldsymbol{E}$ is described by the Boltzmann equation [39]

$$\partial_t f - \frac{e\boldsymbol{E}}{m_e}\partial_{\boldsymbol{v}} f = \partial_t f|_{\text{scatt}}.$$

The term on the right-hand side describes the different scattering processes which randomize the electron distribution. In the case of a vanishing electric field and a nondegenerate system, a Maxwell-Boltzmann distribution results as the equilibrium solution.

A finite electric field $\boldsymbol{E}$ modifies f and induces an electric current. By treating $\boldsymbol{E}$ as a weak perturbation and assuming that the electrons (e) undergo only *binary* collisions with the much heavier ions (i) and neutral particles (n), one can derive the dielectric function

$$\varepsilon^{B}(\omega) = 1 + \frac{2^{3/2}(4\pi e)^2}{3 m_e^{5/2}} \int_0^\infty d\epsilon \, \frac{\epsilon^{3/2}\partial_\epsilon f}{\omega^2 + i\gamma(\epsilon)\omega} \tag{8}$$

of such a system [39]. Here, $\epsilon = m_e \boldsymbol{v}^2/2$ is the kinetic energy of an electron, and

$$\gamma(\epsilon) = |\boldsymbol{v}| n_i \sigma_{ei} + |\boldsymbol{v}| n_n \sigma_{en} \tag{9}$$

is the total rate of electron collisions with ions and neutrals. The respective momentum-transfer cross sections σ_{ei} are determined here from numerical solutions of the Schrödinger equation using statically screened Coulomb interactions [20]. It is interesting to mention that for all relevant velocities and screening lengths, the e-i cross sections obtained that way show quite good agreement with those calculated using classical mechanics [40]. The momentum-transfer cross sections σ_{en} of e-n collisions are taken from Ref. [41].

We emphasize that Eqs. (8) and (9) do not account for e-e scattering. This is an often-applied approximation since a binary e-e collision conserves the total electron momentum and, thus, cannot directly relax the electron current [42].

Figure 6 shows exemplary results of this modeling: In panel (a), the energy-dependent collision rate γ is plotted together with the weighting factor $\epsilon^{3/2}\partial_\epsilon f$ of the integral in Eq. (8) for an electron density of $n_e = 3 \times 10^{17}$ cm^{-3}and an electron temperature of $T_e = 10\,000$ K. Note that γ is large for electrons with kinetic energies below 0.5 eV since slow electrons exhibit large e-i scattering cross sections. However, the weight of these scattering rates is small and rather peaks at about 1 eV where e-n scattering contributes already more than 40% to the total collision rate of $\gamma \approx 5$ THz.

Finally, Fig. 6(b) presents the resulting dielectric function ε^B of a plasma with the same parameters. Note that ε^B exhibits a perfect Drude-like behavior as demonstrated by the best fit to the Drude formula (7). Moreover, the fit accurately reproduces the electron density which was used as an input parameter of Eq. (8). This behavior can be easily understood by inspecting Eq. (8): Electrons with an energy around a

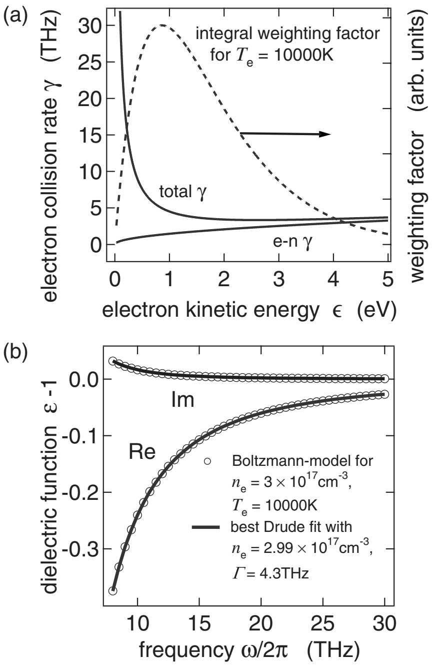

FIG. 6. (a) Collision rate γ of Eq. (9) and weighting factor $\epsilon^{3/2}\partial f_\epsilon$ of the integral in Eq. (8) versus electron energy ϵ for $n_e=3\times10^{17}$ cm^{-3} and T_e=10 000 K. Note that for $\epsilon>1$ eV, e-n scattering starts to dominate the total scattering rate γ. (b) Dielectric function resulting from Eq. (8). Thick solid lines mark a fit according to the Drude formula (7) which excellently reproduces the input electron density.

fixed value ϵ indeed make a Drude-like contribution to the integral. In this sense, the Drude relaxation rate Γ can be interpreted as an averaged collision rate γ,

$$\Gamma=\langle\gamma(\epsilon)\rangle, \tag{10}$$

where the angular brackets indicate an average resulting from a least-square fit of ε^D to ε^B. Accordingly, if the electron collision rate γ does not depend on the electron energy, Eq. (8) precisely reduces to the Drude formula (7) because of $n_e=-(4\pi/3)\int d\epsilon(2\epsilon/m_e)^{3/2}\partial_\epsilon f$ [39].

We conclude that the parametrization of our data by the Drude model is justified both by experiment and by theory, and the two parameters n_e and Γ involved have a clear physical interpretation.

IV. RESULTS AND DISCUSSION

In this section, we discuss the dynamics of the dielectric function of various laser-ionized gases. As shown in the preceding section, this is tantamount to considering the evolution of just two quantities, the electron density n_e and the Drude relaxation rate Γ. Due to its simpler physical interpretation, we start our discussion with n_e which also yields a reliable determination of the electron temperature.

A. Dynamics of the free-electron density

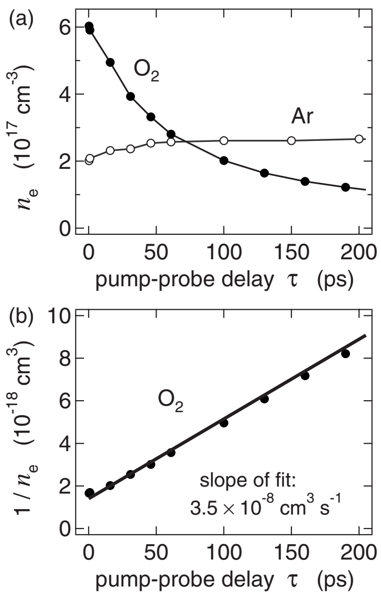

FIG. 7. (a) Temporal evolution of the free-electron density n_e in Ar and O$_2$ following optical ionization. (b) Corresponding dynamics of $1/n_e$ in O$_2$ with a fit to the dissociative-recombination model of Eq. (11).

Figure 7 shows the temporal dynamics of the free-electron density n_e in our laser-ionized gases, both monatomic and molecular. The initial values of $n_e(\tau)$ are compatible with the absorbed pump-pulse energy of $\approx$15 μJ, the estimated plasma volume of 2×10^{-6} cm^3, and the ionization potentials of O$_2$ and Ar.

1. Oxygen: dissociative recombination

In strong contrast to Ar, the electron density in O$_2$ decays on a time scale of approximately 50 ps. This is due to efficient transfer of the released energy of the recombining electron to internal *molecular* degrees of freedom such as vibrations and rotations. In the case of the oxygen plasma, the dissipation of the kinetic and binding energy results in dissociation [43]

$$O_2^+ + e^- \rightarrow O + O^*. \tag{11}$$

With $[O_2^+]=n_e$, the rate equation for this recombination reaction can be written as $\partial_\tau n_e=-\beta n_e^2$. Its solution

$$\frac{1}{n_e(\tau)}=\frac{1}{n_e(0)}+\beta\tau \tag{12}$$

for the inverse electron density is linear in time and excellently reproduces our experimental data for a rate coefficient of $\beta=3.5\times10^{-8}$ cm^3 s^{-1}, as shown in Fig. 7(b). Such a linear behavior was also found on millisecond time scales in experiments with O$_2$ ionized by microwave radiation [44]. Relating our value of β to the recently established phenomenological formula $\beta=2\times10^{-7}\times(T_e/300\text{ K})^{-0.5}$ cm^3 s^{-1} [43] results in an estimate of the electron temperature of at least 10 000 K.

Other reactions like the formation of O_2^- anions do not play a dominant role in the electron decay in our experiment, since they would result in a nonlinear time dependence of $1/n_e$ in contrast to the experimental data in Fig. 7(b). Furthermore, formation of O_2^- anions would imply additional scattering partners for the electrons and thus an *in*creasing Γ with *de*creasing n_e. As shown by Fig. 9(b), this is contrary to our findings.

2. Argon: long-lived electrons

The electron dynamics in the case of Ar are entirely different; n_e still increases during the first 50 ps after the plasma generation, as shown in Fig. 7(a). These additional free electrons at early times are most likely generated by impact ionization of pre-excited Ar atoms by fast electrons [6,39]. The n_e maximum of 2.6×10^{17} cm^{-3} at $\tau = 50$ ps corresponds to about 1% of the total particle density of a gas under normal conditions.

After the initial increase, the electron density remains nearly constant up to $\tau = 200$ ps. These extremely long-lived electrons are typical for monatomic gases and are also observed for the noble gas Kr (data not shown). Although *binary* collisions are the most frequent interaction events, they are very ineffective for the recombination of an Ar^+ ion with an electron due to a lack of effective dissipation channels for the energy of the recombining electron: Momentum conservation dictates that only a fraction $\sim m_e/m_i \sim 10^{-4}$ of the electron energy is converted into kinetic energy of the ion having a much larger mass m_i.

For this reason, the recombination is dominated by the less frequent *three-body* collision [39,45]

$$Ar^+ + 2e^- \rightarrow Ar + e^-. \tag{13}$$

A coarse estimate of the electron temperature T_e in the Ar plasma may be obtained using the rate equation $\partial_\tau n_e = -K n_e^3$ based on Eq. (13) and $n_e = [Ar^+]$. With the reaction constant given by the phenomenological relation $K = 4.2 \times 10^{-29} \times (T_e/10\,000\text{ K})^{-8.29}$ cm^6 s^{-1} [45], one infers that T_e in Ar must be significantly larger than 5000 K. In any case, we expect the electron temperature in the Ar plasma to be similar to that in O_2 in the 10 000 to 20 000 K range.

Finally, it should be mentioned that, in principle, also spontaneous photon emission or sequential reactions like $Ar^+ + 2\,Ar \rightarrow Ar_2^+ + Ar$ followed by $Ar_2^+ + e^- \rightarrow Ar + Ar^*$ can lead to an electron decay. However, $\partial_\tau n_e$ scales with n_e for this reaction in contrast to n_e^3 for Eq. (13). Consequently, the role of Ar_2^+ in the overall electron recombination process becomes negligible at sufficiently high electron densities which is the case in our experiment [45].

3. SF_6 in Argon: electronic temperature

The rough estimates of the electron temperature in the O_2 and Ar plasma are verified by adding a small fraction of the electron scavenger SF_6 to the Ar gas. The free-electron decay in such a mixture is drastically accelerated and dominated by the electron-attachment reaction

$$SF_6 + e^- \rightarrow A^- + R \tag{14}$$

to some anion A^- and remainder R. For example, as demonstrated in Fig. 8, substitution of just 10% of the Ar atoms by SF_6 molecules leads to an ultrafast *mono-exponential* decay of the free electrons with a $1/e$ time of 79 ps. In pure SF_6, this time constant reduces to 12 ps which impressively underlines the effectiveness of SF_6 as an electron scavenger.

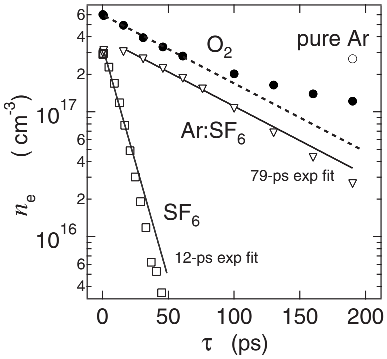

FIG. 8. Logarithmic plot of $n_e(\tau)$ for the 9:1-Ar:SF_6 mixture and pure SF_6 together with mono-exponential fits. The free-electron decay in O_2 deviates considerably from a mono-exponential behavior as demonstrated by comparison to the dashed line. The "O" indicates the value of $n_e(\tau)$ in the Ar plasma, which is largely constant for $\tau > 50$ ps.

The measured decay times allow to reliably derive the electronic plasma temperature to values of $\approx 20\,000$ K [10] since the cross sections for the reaction of Eq. (14) are very well known for a broad range of electron kinetic energies [3]. Using these cross sections in conjunction with the Boltzmann equation shows that the electron-attachment rate decreases strongly with increasing electron temperature T_e, thus providing a sensitive measure of T_e. Note that this method of temperature determination is virtually insensitive to systematic errors in the electron density, since the rate constants inferred only rely on the density ratio $n_e(\tau)/n_e(0)$ [10].

B. Electron collision rate

1. Experimental versus modeled values

Finally, we turn to the dynamics of the electron collision rate Γ shown in Fig. 9(a) for Ar and O_2. The peak values of $\Gamma \approx 25$ THz are comparable to the Drude relaxation rates in metals like Cu and Au with electron densities five orders of magnitude higher than in our plasmas [35]. Figure 9(b) plots $\Gamma(\tau)$ versus $n_e(\tau)$ and reveals that Γ increases nearly linearly with n_e. According to Eqs. (9) and (10), and since the number of neutral particles in gases with low ionization degree like in our experiment is virtually constant, the linear increase of Γ with n_e suggests that e-i collisions are the main contribution to the electron-velocity randomization.

For a microscopic modeling of the Drude relaxation rates Γ, we use the microscopic Boltzmann approach of Sec. III B to calculate Γ as a function of the electron density at several electron temperatures. Figure 9(b) demonstrates that the collision rates Γ obtained this way are about 5 times smaller than those extracted from the experimental data at an electron temperature of 15 000 K. Agreement with the measured Γ values of both the Ar and the O_2 plasma is only reached for unrealistically low electron temperatures of about 2000 K which is one order of magnitude smaller than the experimentally derived values, see Sec. IV A 3.

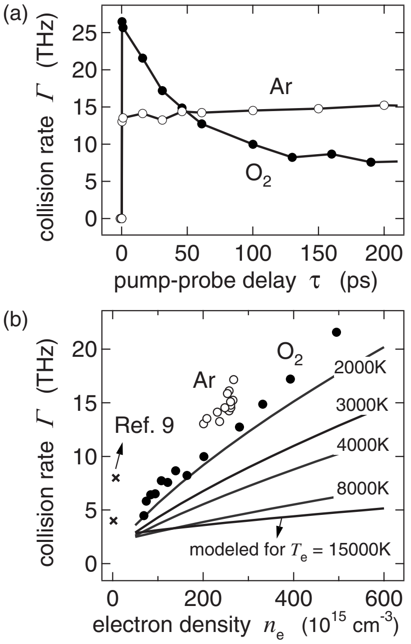

FIG. 9. (a) Temporal dynamics of the Drude collision rate Γ in laser-ionized Ar and O_2. (b) Corresponding plots of the Drude relaxation rate Γ in O_2 and Ar as a function of the electron density n_e. Exemplary Drude relaxation rates of Ref. [9] taken for an O_2 plasma with lower n_e are appended. Solid lines are modeled collision rates at various electron temperatures according to the theoretical approach of Sec. III B.

2. Discussion

What is the reason for the large discrepancy between the measured and modeled relaxation rates Γ?

First of all, we emphasize that our procedure to extract the plasma's dielectric function is based on valid approximations and experimentally verified assumptions as detailed in Sec. II D. We estimate that the extracted free-electron densities n_e and collision rates Γ are correct within a possible systematic error of less than 20%. In addition, Mics *et al.* have performed an experiment similar to ours in the frequency range from 1 to 3 THz using a cylindrical plasma [9]. They as well find a Drude-like dielectric function and relaxation rates Γ that are compatible with ours as shown in Fig. 9(b).

Moreover, we also believe that our determination of the electronic temperature T_e by adding small amounts of SF_6 to the Ar gas is reliable: (i) The derivation of the quantitative relationship between free-electron decay rate and T_e relies on simple rate equations for the electron distribution [10]. They reflect the simple structure of the Boltzmann collision integral which is more complicated in the theory of electric conduction. (ii) The cross sections for electron attachment to SF_6 are very well known [3]. (iii) The high Γ values are observed already directly after plasma generation where a possible electron cooling is completely negligible. For example, the Spitzer formula [22,23] predicts an electron cooling on the nanosecond time scale for the conditions in our Ar plasma. (iv) Last but not least, as shown in Sec. IV A 3 and Ref. [10], our method yields comparable temperatures for differing SF_6 concentrations which are also compatible with the rough estimates of $T_e > 10\,000$ K obtained from the free-electron decay in pure Ar and O_2.

It is instructive to compare the THz conductivity of our Ar plasma to the dc conductivity of steady-state plasmas with comparable free-electron density n_e and temperature T_e. For example, for an Ar plasma with $n_e = 6 \times 10^{17}$ cm^{-3} and $T_e = 16\,400$ K, the dc conductivity from Ref. [46] implies a Drude relaxation rate of merely 2 THz which is much smaller than the 15 THz found from the THz conductivity of our Ar plasma at 2.6×10^{17} cm^{-3} and 20 000 K. The reason for this large discrepancy must lie in the differing experimental details which are discussed in the following.

First, the probe frequencies of 0 THz from Ref. [46] and ~10 THz in our experiment are very different but not expected to lead to strongly differing Drude relaxation rates. In general, quantum-mechanical linear-response theory based on the Kubo formula involves dynamic screening of the bare Coulomb interaction quantified by the inverse dielectric function $1/\varepsilon$. This leads to an enhanced electron collision frequency around the plasma frequency Ω_{pl} because of a coupling to plasma oscillations [47]. However, the large Im ε of our plasmas extremely broadens the plasmon resonance [48] in agreement with the frequency-independent collision rates that are derived from calculated laser-heating rates [49]. This conclusion allows for a direct comparison of Γ taken at zero and at THz frequencies and, moreover, justifies the use of static screening in the theoretical treatment of the plasma conductivity in Sec. III B.

Second and in contrast to our laser-pulse generated plasma, the plasma from Ref. [46] is produced by continuous heating with microwave radiation. However, after electron thermalization on a subpicosecond time scale, one has a Maxwell-Boltzmann distribution for the electrons in both cases. Although the ions in the steady-state plasma are much hotter than those in our plasmas, they are still much slower than the electrons. Therefore, the ions can be considered as static in both cases.

Finally, the linear spatial dimensions of the steady-state plasma in Ref. [46] are of the order of 1 mm whereas our plasmas extend to ~10 μm only. Strong spatial gradients can lead to a modified light absorption, for example due to the build up of an ion-acoustic turbulence [50]. The latter is driven by temperature gradients leading to transport of hot electrons out of the plasma center and a return current of colder electrons. In fact, we find large Knudsen numbers for our plasmas indicating strongly turbulent behavior [51]. The resulting increase of the electron scattering rate is, however, only in the range of a few THz, still insufficient to reproduce the experimental values for the electron collision rate.

Nevertheless, we believe that the large Drude relaxation rates Γ found in our experiment are a result of the strong spatial gradients in the plasma, possibly in combination with other processes that are not included in the theoretical treatment based on the Boltzmann equation in Sec. III B. One example of those is e-e scattering which is expected to contribute up to 40% to the Drude relaxation rate in spatially homogeneous plasmas [42].

V. CONCLUSION AND OUTLOOK

In conclusion, we employed time-resolved THz spectroscopy to study the electron dynamics in optically ionized Ar and O_2 gases. This unique experimental method allows us to access the ultrafast dynamics of the free-electron density and collision rate thereby demonstrating its great capabilities for plasma diagnostics.

The free electrons in O_2 are found to recombine much faster than in Ar since the energy of the recombining electron is dissipated efficiently by the O_2 molecule's rotational and vibrational degrees of freedom. The resulting free-electron decay according to Eq. (12) has important consequences for the triggering of lightnings in the atmosphere by laser pulses [2]: Regardless of the energy of the laser pulse generating the plasma at time $\tau = 0$, the free-electron density cannot exceed $1/\beta\tau$ which amounts to less than 3×10^{13} cm^{-3} after ~ 1 μs which is the time it takes the laser pulse to travel from the ground to the cloud. This calls for other excitation strategies to produce a long and conducting plasma channel between the ground and the charged cloud. A possible solution may employ a sequence of individually shaped laser pulses in which each pulse ionizes the air in a certain height, the first pulse near to the cloud and the last one close to the ground. However, such pulse trains require very strong lasers and special pulse shapers which are not yet available.

Adding a small amount of the electron scavenger SF_6 to an Ar plasma reduces the electron lifetime in the plasma dramatically, which impressively demonstrates the effectiveness of SF_6 as an electron scavenger. The well-known cross sections of this reaction allow us to determine the electron temperature to about 20 000 K.

The free-electron collision rate Γ is found to increase nearly linearly with the electron density n_e and is as large as 25 THz for $n_e = 6 \times 10^{17}$ cm^{-3}. Γ is, for example, relevant for the generation of high harmonics and THz radiation via laser ionization of gases where the strong laser field pulls a bound electron out of the Coulomb potential of the nucleus and accelerates it [17]. The resulting coherent current is maintained until the electron velocity is randomized by collisions at a rate Γ. In this way, Γ affects the magnitude and shape of the generated current bursts. Our measured values of $\Gamma \approx 25$ THz are in between the somewhat unrealistic values of 1 and 1000 THz assumed in Refs. [52,53], respectively, to model the emitted THz radiation.

A state-of-the-art theoretical calculation of the measured Drude relaxation rates Γ based on the Boltzmann equation yields rates half an order of magnitude smaller than those derived from the experiment. This is particularly surprising for Ar, a prototypical electron-ion system, where all relevant scattering processes should be well understood. Comparison to dc-conductivity measurements of steady state plasmas strongly suggests that the high collision rates in our plasma are related to its large spatial gradients.

Future theoretical efforts have to include additional relaxation processes to explain the high electron collision rates observed. On the experimental side, measurements for different plasma profiles have to be performed to quantify the effect of spatial gradients. In addition, applying much higher pump intensities should lead to a significant part of doubly charged ions. New pathways for the free-electron decay and different electron scattering can be expected in this regime. Also, the investigation of other gases such as H_2, N_2, and gaseous H_2O seems promising. Finally, the subpicosecond dynamics directly after plasma generation should exhibit signatures of the build up of electron correlations as recently observed in electron-hole plasmas in semiconductors [48].

ACKNOWLEDGMENTS

We thank K. Reimann, P. Hilse, S. Kosse, and G. K. Grubert for enlightening discussions and tests with their programs. One of us (L.P.) gratefully acknowledges support from the Marie Curie Program. In part, this work was financially supported by the Deutsche Forschungsgemeinschaft through Sonderforschungsbereich 450 and 652 and the United Kingdom's Engineering and Physical Sciences Research Council.

APPENDIX A: MODIFIED WKB APPROXIMATION

We rewrite the one-dimensional wave equation (4) as

$$[\partial_z^2 + k^2(z,\omega)]E(z,\omega) = 0, \tag{A1}$$

where we have omitted the index τ denoting the pump-probe delay for clarity. This equation has the same structure like the one-dimensional stationary Schrödinger equation and can be solved approximately by the approach of Wentzel, Kramers, and Brillouin (WKB). Here, the electric field is represented as

$$E = \exp(\mathrm{i}s) \tag{A2}$$

with a complex phase $s(z,\omega)$. Inserting Eq. (A2) into Eq. (A1) leads to

$$(\partial_z s)^2 = k^2 + \mathrm{i}\partial_z^2 s \tag{A3}$$

which is still entirely general and equivalent to Eq. (A1).

In the case of a spatially homogeneous medium with a constant $k = k_0$, the exact solution of Eq. (4) is a superposition of a forward- and a backward-propagating plane harmonic wave $\exp(\mathrm{i}k_0 z)$ and $\exp(-\mathrm{i}k_0 z)$, respectively. This corresponds to a constant $\partial_z s = \pm k_0$ implying $\partial_z^2 s = 0$.

If now k starts to vary weakly over a local wavelength $2\pi/k$, the same holds true for $\partial_z s$, and the second derivative $\partial_z^2 s$ can be considered as a perturbation in Eq. (A3). To lowest order, this yields $\partial_z s = \pm k$ and the usual WKB solution

$$E = A_+ \exp\left[\mathrm{i}\int \mathrm{d}z k\right] + A_- \exp\left[-\mathrm{i}\int \mathrm{d}z k\right] \tag{A4}$$

with complex coefficients A_+ and A_- for the forward- and backward-propagating wave. It represents a good approximation to the two-dimensional solution space of Eq. (A1) if $|\partial_z^2 s| \ll |k^2|$. According to (A4), this condition is equivalent to

$$|\partial_z k| \ll |k^2|,$$

that is, k must exhibit only small relative changes over a length $|1/k|$. Note that Eq. (A4) approximates the *total* electric field $E = E_\infty + \Delta E$. Here, we are, however, interested in a good approximation to the pump-induced *changes* ΔE.

To this end, we consider a wave solely forward propagating through the unexcited sample, $\partial_z s_\infty = +k_\infty$, which is fulfilled in our experiment since no reflections occur in the unexcited gas. Excitation by the pump pulse induces changes $\Delta k = k - k_\infty$ and $\Delta s = s - s_\infty$. Equation (A3) then becomes

$$(k_\infty + \partial_z \Delta s)^2 = k^2 + \mathrm{i}\partial_z^2 \Delta s \approx \left[k + \frac{\mathrm{i}\partial_z^2 \Delta s}{2k} \right]^2,$$

where the approximation is valid for $|\partial_z^2 \Delta s| \ll |4k^2|$. When applying the square root to this relation, the negative root can be ruled out since it does not fulfill the boundary condition $\Delta s = 0$ if $\Delta k = 0$. This, in turn, leads to

$$\partial_z \Delta s = \Delta k + \frac{\mathrm{i}\partial_z^2 \Delta s}{2k} \approx \Delta k, \tag{A5}$$

where the last step presumes $|\partial_z^2 \Delta s| \ll |2k\Delta k|$. Therefore, the pump-induced change ΔE in the THz electric field normalized to the electric field E_∞ of the unexcited sample becomes

$$\frac{\Delta E(z,\omega)}{E_\infty(z,\omega)} = \exp\left[\mathrm{i} \int_{-\infty}^{z} \mathrm{d}z' \Delta k(z',\omega) \right] - 1. \tag{A6}$$

This modified WKB approximation is completely analogous to the ordinary WKB approximation of Eq. (A4) but expected to be good under slightly different conditions,

$$|\partial_z \Delta k| \ll |4k^2| \quad \text{and} \quad |\partial_z \Delta k| \ll |2k\Delta k|. \tag{A7}$$

Here, we have used Eq. (A5) to rewrite all the assumptions made to arrive at Eq. (A6).

We check the validity of Eq. (A6) for our plasma by using the refractive index $n = \sqrt{\varepsilon} = ck/\omega$ and $\partial_z \Delta n \approx \Delta n(z = 0,\omega)/d_{\mathrm{pl}}$ where $d_{\mathrm{pl}} \approx 15\ \mu\mathrm{m}$ is the effective plasma thickness, see Appendix B. Then Eq. (A7) becomes

$$|\lambda \Delta n| \ll |8\pi n d_{\mathrm{pl}}| \quad \text{and} \quad |\lambda| \ll 4\pi d_{\mathrm{pl}}, \tag{A8}$$

where the first condition is easily fulfilled in our plasma even at $\omega/2\pi = 10$ THz, $|\Delta n| = 0.3$, and the resulting wavelength $|\lambda| = |2\pi c/\omega n| \approx 30\ \mu\mathrm{m}$. The second condition in Eq. (A8) requires $|\lambda|$ to be substantially smaller than $4\pi d_{\mathrm{pl}} \approx 200\ \mu\mathrm{m}$ which is still valid at 10 THz.

It is important to note that we have also checked the applicability of the modified WKB approximation by solving Eq. (A1) numerically for a broad variety of spatial profiles $\Delta k(z,\omega)$ including, for example, narrow Gaussian profiles. In all cases, the numerical solutions results deviate only by less than 2% from the WKB-derived Eq. (A6).

APPENDIX B: SPATIAL INHOMOGENEITY

Taking the logarithm of Eq. (A6) yields the pump-induced change $\int \mathrm{d}z \Delta n$ in the refractive index, but spatially averaged over regions with different electron density, temperature and so on. How can one deal with the unknown spatial structure of the plasma along the z axis in Fig. 1 and extract local plasma properties, for example in the plasma center at $z = 0$?

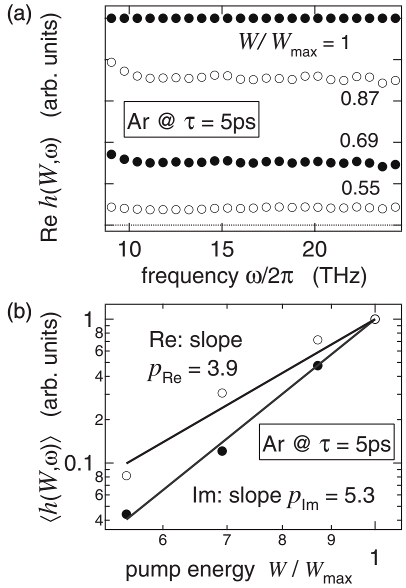

FIG. 10. (a) Spectral dependence of the auxiliary quantity h of Eq. (B2) measured in Ar at 5 ps after excitation with different pump-pulse energies W. The maximum pulse energy of $W_{\mathrm{max}} = 0.4$ mJ corresponds to a maximum intensity of $\approx 2 \times 10^{13}\ \mathrm{W\,cm^{-2}}$ in the center of the pump focus. (b) Dependence of the spectrally averaged $h(W,\omega)$ on the pump intensity together with power law fits in double-logarithmic presentation.

As long as transport effects can be neglected, the spatial variation of Δn should be determined by the locally deposited amount of pump-pulse energy, that is, $\Delta n(z,\omega) = \Delta n[I_{\mathrm{pump}}(z),\omega]$. Moreover, we tentatively assume a power law for the change in the refractive index with respect to the pump intensity,

$$\mathrm{Re}\,\Delta n \propto I_{\mathrm{pump}}^{p_{\mathrm{Re}}}, \quad \mathrm{Im}\,\Delta n \propto I_{\mathrm{pump}}^{p_{\mathrm{Im}}}. \tag{B1}$$

It is instructive to introduce the auxiliary quantity

$$h(W,\omega) := \int \mathrm{d}z \Delta n(z,\omega) = \frac{c}{\mathrm{i}\omega} \ln \frac{S}{S_\infty}, \tag{B2}$$

where we have used Eqs. (A6) and (6) to switch to the experimentally measured signals S and S_∞. According to the ansatz of Eq. (B1), Re h and Im h should obey the corresponding power law with respect to the pump pulse energy W,

$$\mathrm{Re}\,h(W,\omega) \propto W^{p_{\mathrm{Re}}}, \quad \mathrm{Im}\,h(W,\omega) \propto W^{p_{\mathrm{Im}}}. \tag{B3}$$

Indeed, as seen in Fig. 10(a) for Ar at $\tau = 5$ ps after excitation, the left-hand side of Eq. (B3) does *not* depend on frequency. Moreover, Fig. 10(b) shows that it can be adequately described by a power law with exponents $p_{\mathrm{Re}} = 3.9$ and $p_{\mathrm{Im}} = 5.3$, respectively. We conclude that the ansatz of Eq. (B1) for the spectral shape of the pump-induced change Δn in the refractive index is very reasonable. For O_2, we find exponents of $p_{\mathrm{Re}} = 2.9$ and $p_{\mathrm{Im}} = 4.5$; the exponents for SF_6 are assumed to agree with those of Ar because of the nearly equal ionization potential.

We now put Eqs. (1), (B2), and (B1) together to finally obtain

$$\mathrm{Re}\left[\frac{c}{\mathrm{i}\omega} \ln \frac{S}{S_\infty} \right] = \frac{w}{\sqrt{0.88 p_{\mathrm{Re}}}} \mathrm{Re}\,\Delta n(z = 0,\omega) \tag{B4}$$

and an analog expression for the imaginary part which both allow for the extraction of the dielectric function $\varepsilon = (1$

$+\Delta n)^2$ at the center $z=0$ of the pump-induced plasma.

As suggested by Eq. (B4), $w/\sqrt{0.88 p_{\mathrm{Re}}}$ or $w/\sqrt{0.88 p_{\mathrm{Im}}}$ can be understood as an effective plasma thickness d_{pl} which amounts to roughly 15 μm for all gases investigated. As discussed in Sec. II B 2, this value is large compared to the plasma-expansion lengths expected during the first 200 ps after plasma generation, and the presented analysis should remain valid there as well.

[1] X. M. Zhao, J. C. Diels, C. Y. Wang, and J. M. Elizondo, IEEE J. Quantum Electron. **31**, 599 (1995).

[2] J. Kasparian, M. Rodriguez, G. Méjean, J. Yu, E. Salmon, H. Wille, R. Bourayou, S. Frey, Y.-B. André, A. Mysyrowicz, R. Sauerbrey, J.-P. Wolf, and L. Wöste, Science **301**, 61 (2003).

[3] L. G. Christophorou and J. K. Olthoff, J. Phys. Chem. Ref. Data **29**, 267 (2000).

[4] B. La Fontaine, F. Vidal, Z. Jiang, C. Y. Chien, D. Comtois, A. Desparois, T. W. Johnston, J.-C. Kieffer, and H. Pépin, Phys. Plasmas **6**, 1615 (1999).

[5] S. Tzortzakis, B. Prade, M. Franco, and A. Mysyrowicz, Opt. Commun. **181**, 123 (2000).

[6] A. E. Martirosyan, C. Altucci, A. Bruno, C. de Lisio, A. Porzio, and S. Solimeno, J. Appl. Phys. **96**, 5450 (2004).

[7] S. P. Jamison, J. Shen, D. R. Jones, R. C. Issac, B. Ersfeld, D. Clark, and D. A. Jaroszynski, J. Appl. Phys. **93**, 4334 (2003).

[8] B. H. Kolner, P. M. Conklin, R. A. Buckles, N. K. Fontaine, and R. P. Scott, Appl. Phys. Lett. **87**, 151501 (2005).

[9] Z. Mics, F. Kadlec, P. Kužel, P. Jungwirth, S. E. Bradforth, and V. A. Apkarian, J. Chem. Phys. **123**, 104310 (2005).

[10] T. Kampfrath, L. Perfetti, D. O. Gericke, C. Frischkorn, P. Tegeder, and M. Wolf, Chem. Phys. Lett. **429**, 350 (2006).

[11] R. Huber, A. Brodschelm, F. Tauser, and A. Leitenstorfer, Appl. Phys. Lett. **76**, 3191 (2000).

[12] Q. Wu and X. C. Zhang, Appl. Phys. Lett. **71**, 1285 (1997).

[13] K. Reimann, R. P. Smith, A. M. Weiner, T. Elsaesser, and M. Woerner, Opt. Lett. **28**, 471 (2003).

[14] T. Kampfrath, J. Nötzold, and M. Wolf, Appl. Phys. Lett. **90**, 231113 (2007).

[15] P. Tournois, Opt. Commun. **140**, 245 (1997).

[16] National Institute of Standards and Technology, Chemistry WebBook. http://webbook.nist.gov/chemistry/

[17] T. Brabec and F. Krausz, Rev. Mod. Phys. **72**, 545 (2000).

[18] J. H. Posthumus, Rep. Prog. Phys. **67**, 623 (2004).

[19] C. Cornaggia and Ph. Hering, Phys. Rev. A **62**, 023403 (2000).

[20] D. O. Gericke, S. Kosse, M. Schlanges, and M. Bonitz, Phys. Rev. B **59**, 10639 (1999).

[21] D. Kremp, M. Schlanges, and W.-D. Kraeft, *Quantum Statistics of Nonideal Plasmas* (Springer, Berlin, 2005).

[22] L. D. Landau, Phys. Z. Sowjetunion **10**, 154 (1936).

[23] L. Spitzer, *Physics of Fully Ionized Plasmas* (Interscience, New York, 1956).

[24] M. W. C. Dharma-wardana and F. Perrot, Phys. Rev. E **58**, 3705 (1998); **63**, 069901(E) (2001).

[25] G. Hazak, Z. Zinamon, Y. Rosenfeld, and M. W. C. Dharma-wardana, Phys. Rev. E **64**, 066411 (2001).

[26] D. O. Gericke, M. S. Murillo, and M. Schlanges, Phys. Rev. E **65**, 036418 (2002).

[27] J. C. Gibson, R. J. Gulley, J. P. Sullivan, S. J. Buckman, V. Chan, and P. D. Burrow, J. Phys. B **29**, 3177 (1996).

[28] M. Dunne, T. Afshar-Rad, J. Edwards, A. J. MacKinnon, S. M. Viana, O. Willi, and G. Pert, Phys. Rev. Lett. **72**, 1024 (1994).

[29] T. Kampfrath, Ph.D. thesis, Freie Universität Berlin, 2006 (http://www.diss.fu-berlin.de/2006/250/index.html).

[30] S. Ichimaru, *Basic Principles of Plasma Physics: A Statistical Approach* (Benjamin, New York, 1973).

[31] J. T. Kindt and C. A. Schmuttenmaer, J. Chem. Phys. **110**, 8589 (1999).

[32] H. Němec, F. Kadlec, and P. Kužel, J. Chem. Phys. **117**, 8454 (2002).

[33] P. Yeh, *Optical Waves in Layered Media* (Wiley, New York, 1988).

[34] T. Kampfrath, L. Perfetti, F. Schapper, C. Frischkorn, and M. Wolf, Phys. Rev. Lett. **95**, 187403 (2005).

[35] N. W. Ashcroft and N. D. Mermin, *Solid State Physics* (Saunders, Philadelphia, 1976).

[36] N. V. Smith, Phys. Rev. B **64**, 155106 (2001).

[37] M. Dressel and M. Scheffler, Ann. Phys. **15**, 535 (2006).

[38] M. van Exter and D. Grischkowsky, Phys. Rev. B **41**, 12140 (1990).

[39] E. H. Holt and R. E. Haskell, *Foundations of Plasma Physics* (Macmillan, New York, 1965).

[40] S. A. Khrapak, A. V. Ivlev, and G. E. Morfill, Phys. Rev. E **70**, 056405 (2004).

[41] M. Mitchner and C. H. Kruger, *Partially Ionized Gases* (Wiley, New York, 1973).

[42] W. A. Stygar, G. A. Gerdin, and D. L. Fehl, Phys. Rev. E **66**, 046417 (2002).

[43] A. Petrignani, W. J. van der Zande, P. C. Cosby, F. Hellberg, R. D. Thomas, and M. Larsson, J. Chem. Phys. **122**, 014302 (2005).

[44] F. J. Mehr and M. A. Biondi, Phys. Rev. **181**, 264 (1969).

[45] A. Bultel, B. van Ootegem, A. Bourdon, and P. Vervisch, Phys. Rev. E **65**, 046406 (2002).

[46] A. Esser and G. Röpke, Phys. Rev. E **58**, 2446 (1998); M. M. Popovic, Y. Vitel, and A. A. Mihajlov, in *Strongly Coupled Plasmas*, edited by S. Ichimaru (Elsevier, New York, 1990).

[47] H. Reinholz, R. Redmer, G. Röpke, and A. Wierling, Phys. Rev. E **62**, 5648 (2000).

[48] R. Huber, F. Tauser, A. Brodschelm, M. Bichler, G. Abstreiter, and A. Leitenstorfer, Nature (London) **414**, 286 (2001).

[49] T. Bornath, M. Schlanges, P. Hilse, and D. Kremp, Phys. Rev. E **64**, 026414 (2001).

[50] S. H. Glenzer, W. Rozmus, V. Y. Bychenkov, J. D. Moody, J. Albritton, R. L. Berger, A. Brantov, M. E. Foord, B. J. MacGowan, R. K. Kirkwood, H. A. Baldis, and E. A. Williams, Phys. Rev. Lett. **88**, 235002 (2002).

[51] W. Rozmus, V. T. Tikhonchuk, V. Y. Bychenkov, and C. E. Capjack, Phys. Rev. E **50**, 4005 (1994).

[52] K. Y. Kim, J. H. Glownia, A. J. Taylor, and G. Rodriguez, Opt. Express **15**, 4577 (2007).

[53] M. Kreß, T. Löffler, M. D. Thomson, R. Dörner, H. Gimpel, K. Zrost, T. Ergler, R. Moshammer, U. Morgner, J. Ullrich, and H. G. Roskos, Nature (London) **2**, 327 (2006).